

Variational Bayes image restoration with compressive autoencoders

Maud Biquard
ISAE-Supaero / CNES
31400 Toulouse, France

maud.biquard@isae-supaero.fr

Marie Chabert
IRIT/INP-ENSEEIH
31000 Toulouse, France

marie.chabert@toulouse-inp.fr

Thomas Oberlin
ISAE-Supaero
31400 Toulouse, France

thomas.oberlin@isae-supaero.fr

Abstract

Regularization of inverse problems is of paramount importance in computational imaging. The ability of neural networks to learn efficient image representations has been recently exploited to design powerful data-driven regularizers. While state-of-the-art plug-and-play methods rely on an implicit regularization provided by neural denoisers, alternative Bayesian approaches consider Maximum A Posteriori (MAP) estimation in the latent space of a generative model, thus with an explicit regularization. However, state-of-the-art deep generative models require a huge amount of training data compared to denoisers. Besides, their complexity hampers the optimization of the latent MAP. In this work, we propose to use compressive autoencoders for latent estimation. These networks, which can be seen as variational autoencoders with a flexible latent prior, are smaller and easier to train than state-of-the-art generative models. We then introduce the Variational Bayes Latent Estimation (VBLE) algorithm, which performs this estimation within the framework of variational inference. This allows for fast and easy (approximate) posterior sampling. Experimental results on image datasets BSD and FFHQ demonstrate that VBLE reaches similar performance than state-of-the-art plug-and-play methods, while being able to quantify uncertainties faster than other existing posterior sampling techniques.

1 Introduction

Image restoration tasks, such as denoising, deblurring, inpainting or super-resolution, consist in recovering a clean image x from its noisy measurement y , based on the forward model $y = Ax + w$, with A representing the degra-

dation operator and w an additive noise term. Within the Bayesian framework, this ill-posed inverse problem is typically solved by finding the Maximum A Posteriori (MAP) estimate, solution to the problem

$$\max_x p_{X|Y}(x|y) \Leftrightarrow \min_x -\log p_{Y|X}(y|x) - \log p_X(x) \quad (1)$$

where $\log p_{Y|X}(y|x)$ is the observation log-likelihood, which is quadratic for Gaussian noise, and $-\log p_X(x)$ acts as a regularization term, promoting solutions that are most compatible with the prior distribution $p_X(x)$. Classical regularizations include total variation [45], Tikhonov regularization [51], and sparsity-promoting penalties on well-chosen representations such as wavelet bases or dictionaries [50, 26, 38].

Deep learning has led to substantial performance gains in image restoration tasks. A first category of methods directly solves the inverse problem after a supervised end-to-end training on a dataset of original-degraded image pairs related by the forward model [22, 46]. Their performance are impressive but only for the specific inverse problem considered during training. For that reason, a second category of methods aims at learning the regularization only, leveraging the forward model to solve the inverse problem. Besides offering a better interpretability, they allow to solve a wide range of inverse problems with the same neural network.

Among them, plug-and-play (PnP) image restoration methods [52] yield excellent performance on a wide variety of image restoration tasks. These methods classically use splitting algorithms, such as ADMM [52, 10] or HQS [55, 31], that separately handle the data term and the regularization term in the optimization problem (1). Their key concept is to use Gaussian denoisers [33], and in particular deep denoisers [56] in place of the proximal operator of the regularization. More recently, the introduction of generative denoisers, such as denoising diffusion models [29, 41],

within the PnP framework, has demonstrated remarkable performance in solving inverse problems [35, 14, 58].

A more direct way to learn the regularization consists in estimating the data distribution within generative models. This line of work, referred to as latent optimization in the following, seeks the inverse problem solution in the latent space of a generative model. Specifically, given a generative model G which has been trained on a dataset of ideal images x_i , the seminal work [6] computes a MAP estimate in its latent space by solving the following optimization problem using gradient descent:

$$\max_z p_{Z|Y}(z|y) \Leftrightarrow \min_z -\log p_{Y|Z}(y|z) - \log p_Z(z), \quad (2)$$

where $p_{Y|Z}(y|z) = p_{Y|X}(y|G(z))$, that is G is considered as a deterministic transformation from the latent to the image space, and $p_Z(z)$ is the generative latent prior. The original approach introduced in [6] is efficient for solving severely ill-posed inverse problems on images lying on a low-dimensional manifold, such as centered close-ups on human faces. Unfortunately, the manifold constraint $x = G(z)$ too strongly restricts the solution space when dealing with images lying on a high-dimensional manifold, which is the case for highly diverse and/or non-structured images, or when solving less severely ill-posed inverse problems. To address this limitation, [19, 18] permit small deviations from the generative manifold while [27, 23, 24] propose to jointly optimize x and z using splitting algorithms. Solving eq. (2) using Normalizing Flows (NF) [21] is also an option as it ensures the accessibility of any element in the image space [1, 42]. Even so, the quality of the solution remains highly dependent on the generative model. Unfortunately, the use of very deep state-of-the-art generative models makes the optimization of eq. (2) problematic. Indeed, the gradient descent often gets trapped in poor local minima [16] and it can be regarded as too computationally demanding for restoring a single image. Moreover, the training of very deep generative models require a lot of ideal images, which might not be accessible in some application contexts. In order to circumvent gradient descent, [27] uses the encoder of a variational autoencoder (VAE) as a stochastic approximate of the generative model posterior $p(z|x)$ in an alternate optimization scheme on (x, z) , while [44] obtains promising performance by extending this approach to hierarchical VAEs [48], at the cost of additional image restoration hyperparameters.

All the above mentioned methods only provide a single point estimate of the inverse problem solution. However, in many applications, the quantification of image uncertainty is a key requirement. To this end, several Bayesian methods enable to sample the posterior distribution $p_{X|Y}(x|y)$ of the inverse problem solution. Some methods yield stochastic solutions to the inverse problem, relying, for instance, on the implicit prior provided by Gaussian denoisers

[32] or exploiting diffusion model properties [58]. However, posterior sampling is then computationally expensive since the inverse problem must be solved for each sample generation. In this regard, Markov Chain Monte Carlo (MCMC) can lead to more effective techniques. In particular, [25] proposes to use Unadjusted Langevin Algorithm (ULA) to solve imaging inverse problems. Building on this, PnP-ULA [37] approximates the log-likelihood gradient in ULA by employing a Gaussian denoiser in a plug-and-play framework. NF-ULA [9] directly approximates this gradient using normalizing flows while [30] uses a MCMC sampling scheme in the latent space of a generative model. Many of these methods offer theoretical convergence guarantees towards the actual posterior distribution. However it requires in practice many iterations which makes the restoration computationally heavy, despite recent attempts to speed up Markov chains convergence [15, 43]. Additionally, convergence is conditioned to the tuning of sensitive hyperparameters. Consequently, these methods often struggle to reach the state-of-the-art performance and computational efficiency achieved by their point estimate counterparts, although yielding valuable uncertainty quantification.

Focusing on latent optimization methods, this paper addresses the issues arising when dealing with diverse or non-structured images. Moreover, taking benefit of the latent framework, the proposed approach offers an efficient means to quantify the uncertainty. Hence, our contribution is twofold: first, we propose compressive autoencoders (CAEs) [3] as an alternative to state-of-the-art generative models for latent optimization methods. We consider in particular CAEs with a hyperprior [4], which yield excellent results in compression and can be seen as VAEs with an adaptive latent prior. In addition, they are significantly smaller than state-of-the-art generative models. On one hand, their adaptability allows to properly regularize inverse problems on non-structured images. On the other hand, their light structure makes the latent optimization using gradient descent [6] both scalable and effective. Second, we introduce the Variational Bayes Latent Estimation (VBLE) algorithm which estimates $p_{Z|Y}(z|y)$ by variational inference, making a stochastic version of the gradient descent used to solve eq. (2). VBLE enables to estimate the posterior distribution with negligible additional computational cost.

We conduct a comprehensive set of experiments such as deblurring, single image super resolution (SISR) and inpainting on FFHQ [34] and BSD [39] datasets. The proposed approach yields competitive image restoration results compared to state-of-the-art methods. It additionally provides relevant uncertainty estimates compared to MCMC methods, with an algorithm being significantly faster.

2 Background

2.1 Variational autoencoders

VAEs are composed of an encoder, known as the inference model as it approximates the unknown posterior distribution, and of a decoder used as a generative model [36]. Both are neural networks, whose weights, ϕ and θ respectively, are learned using variational inference [5]. Let the image x depend on a latent variable z according to the following generative model:

$$p_\theta(x, z) = p_\theta(x|z)p_\theta(z). \quad (3)$$

$p_\theta(z)$ is typically a simple distribution, often chosen as $\mathcal{N}(0, I)$, while $p_\theta(x|z)$ is the mapping from the latent to the image spaces learned by the decoder. The posterior distribution, defined as

$$p_\theta(z|x) = \frac{p_\theta(x|z)p_\theta(z)}{\int_z p_\theta(x|z)p_\theta(z)} \quad (4)$$

is often intractable and is approximated by $q_\phi(z|x)$, the inference model produced by the VAE encoder.

The weights θ and ϕ are learned during the training of the VAE by maximizing the Evidence Lower Bound (ELBO):

$$\mathcal{L}_{\theta, \phi}(x) = \log p_\theta(x) - KL(q_\phi(z|x)||p_\theta(z|x)) \quad (5)$$

where KL denotes the Kullback-Leibler divergence, measuring the distance between distributions. Hence, by maximizing the ELBO on a dataset \mathcal{D} containing several images x , the log-likelihood of \mathcal{D} is maximized, while the distance between the approximate and true posterior distributions is minimized. However, this version of the ELBO is intractable as it depends on the posterior $p_\theta(z|x)$. Yet, the ELBO can be rewritten as follows:

$$\mathcal{L}_{\theta, \phi}(x) = \mathbb{E}_{q_\phi(z|x)} [\log p_\theta(x|z) + \log p_\theta(z) - \log q_\phi(z|x)], \quad (6)$$

$$= \mathbb{E}_{q_\phi(z|x)} [\log p_\theta(x|z)] - KL(q_\phi(z|x)||p_\theta(z)). \quad (7)$$

The tractable version of the ELBO in eq. (7) consists of two terms. The first one is a data fidelity term which ensures a good reconstruction of the input x by the autoencoder. The second one encourages the latent space to match the shape of the prior distribution $p_\theta(z)$. The ELBO formulations of Eqs. (6) and (7) are used to update (θ, ϕ) because they yield tractable estimates of $\mathcal{L}_{\theta, \phi}(x)$ and of its gradient. Indeed, leveraging the reparametrization trick, two Stochastic Gradient Variational Bayes (SGVB) ELBO estimates can be de-

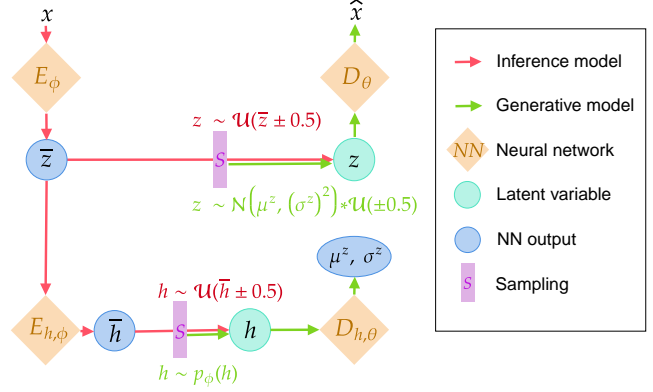


Figure 1. Structure of a compressive autoencoder with hyperprior as in [4]. All mentioned distributions are factorized, in particular $\mathcal{N}(\mu^z, (\sigma^z)^2) * \mathcal{U}(\pm 0.5) = \prod_k [\mathcal{N}(\mu_k^z, (\sigma_k^z)^2) * \mathcal{U}(-0.5, 0.5)]$.

rived [36] by differentiating the following losses:

$$\tilde{\mathcal{L}}_{\theta, \phi}^A(x) = \frac{1}{L} \sum_{i=1}^L [\log p_\theta(x|z_i) + \log p_\theta(z_i) - \log q_\phi(z_i|x)] \quad (8)$$

$$\tilde{\mathcal{L}}_{\theta, \phi}^B(x) = \frac{1}{L} \left[\sum_{i=1}^L \log p_\theta(x|z_i) \right] - KL(q_\phi(z|x)||p(z)) \quad (9)$$

where $z_i \sim q_\phi(z|x)$ for $i = 1, \dots, L$. The estimate (9) yields typically less variance than (8), but can only be used when $KL(q_\phi(z|x)||p(z))$ has a closed form. It is the case when the prior and approximate posterior distributions are Gaussian, but not in general. Finally, (θ, ϕ) can be learned by applying SGD (Stochastic Gradient Descent) to $\tilde{\mathcal{L}}_{\theta, \phi}^A$ or to $\tilde{\mathcal{L}}_{\theta, \phi}^B$. In practice, only one sample is used to estimate the ELBO expectation for a given $x \in \mathcal{D}$, i.e. $L = 1$ in Eqs. (8) and (9).

2.2 Variational compressive autoencoders

Machine learning and especially deep learning have raised a significant interest in the lossy image compression community. In the widespread transform coding framework, the image is transformed, the obtained image representation is quantized and subsequently compressed using a lossless entropy encoder [54]. The more decorrelated and sparse the transform is, the more effective the compression becomes. Several reference model-based methods use the wavelet transform [47] while state-of-the-art deep learning methods use data-dependent transforms provided by the encoder part of a compressive autoencoder (CAE) [3, 4, 40, 12]. CAEs are learned by minimizing a rate-distortion trade-off $\mathcal{L} = \text{Rate} + \alpha \times \text{Distortion}$ [3, 4]. On one hand, the quantization introduces distortion between the original and the de-

compressed image. This distortion is typically measured by the Mean Squared Error (MSE) between the network input and output. On the other hand, the entropy encoder design assumes a prior distribution or so-called entropy model p for the quantized latent representation, denoted by z in the following. However, z actual distribution, denoted by q , generally differs from p . The rate is approximated by the Shannon cross entropy: $\text{Rate} = \mathbb{E}_{z \sim q}[-\log_2 p(z)]$. This value is minimized when $p = q$, that is when the rate corresponds to the information entropy.

A specificity of CAE training comes from the fact that quantization is non-differentiable. It is thus approximated during training by the addition of a uniform noise, which classically models quantization noise [7]. This noise is akin to the noise introduced during the training of a VAE in the generative framework. In the following, we denote by \bar{z} the representation before the quantization. The latent variable z is thus a noisy version of \bar{z} . Furthermore, state-of-the-art CAEs incorporate a hyperprior [4, 40, 11]. This additional autoencoder takes \bar{z} as input and estimates z 's mean μ^z and standard deviation σ^z , as illustrated in Fig. 1. The prior on z is then defined as the \bar{z} -dependent factorized distribution $\prod_k \mathcal{N}(\mu_k^z, (\sigma_k^z)^2)$, convolved by a uniform distribution to align with quantization. The hyperprior introduces another latent variable h , of much smaller dimension than z . h is also compressed quantized, entropy coded and transmitted.

CAEs can be formulated as VAEs [3, 4], with particular generative and inference models. Consider the following generative model, corresponding to a CAE with a hyperprior:

$$p_\theta(x, z, h) = p_\theta(x|z)p_\theta(z|h)p_\theta(h) \quad (10)$$

$$\begin{aligned} \text{with } p_\theta(x|z) &= \prod_k \mathcal{N}(x_k; D_\theta(z)_k, \frac{1}{2\alpha \log(2)}), \\ p_\theta(z|h) &= \prod_k \left[\mathcal{N}(z_k; \mu_k^z, (\sigma_k^z)^2) * U(z_k; [-\frac{1}{2}, \frac{1}{2}]) \right], \\ p_\theta(h) &= \prod_k p_\psi(h_k), \end{aligned}$$

where D_θ represents the decoder part of the autoencoder, and p_ψ denotes a factorized parametric prior with weights ψ learned during training. Consider also the following inference model:

$$\begin{aligned} q_\phi(z, h|x) &= q_\phi(z|x, h)q_\phi(h|x) \quad (11) \\ \text{with } q_\phi(z|x, h) &= \prod_k \mathcal{U}(z_k; [\bar{z}_k - \frac{1}{2}, \bar{z}_k + \frac{1}{2}]), \\ q_\phi(h|x) &= \prod_k \mathcal{U}(h_k; [\bar{h}_k - \frac{1}{2}, \bar{h}_k + \frac{1}{2}]). \end{aligned}$$

Then, the ELBO from eq. (6), expressed for a hierarchical VAE with two latent variables, corresponds to the rate-

distortion loss, up to a $\log(2)$ factor:

$$\begin{aligned} \mathcal{L}(x) &= \mathbb{E}_{q_\phi(z, h|x)} \left[\log q_\phi(z, h|x) - \log p_\theta(x|z, h) \right. \\ &\quad \left. - \log p_\theta(z, h) \right] \quad (12) \\ &\propto 0 + \log(2)(\alpha \text{Distortion}(x, z) + \text{Rate}(z, h)), \end{aligned}$$

if the expectation is approximated using a single Monte Carlo sample, as is done in VAE training. Finally, CAEs are powerful neural networks, while remaining often scalable, as they are to be used in embedded systems [17]. In particular, these networks use a parametric activation function, known as Generalized Divisive Normalization [2] (GDN), which permits a good approximation quality for natural images with fewer layers than classical neural networks.

3 Contributions

3.1 Regularization with compressive autoencoders

We claim that CAEs, introduced in Sec. 2.2, are good candidates to be used when restoring images with latent optimization methods. First, they can be viewed as VAEs and may be employed similarly. Second, they remain relatively light as their structure has been optimized for embedded image processing, enabling the use of gradient descent to compute the MAP- z estimate of eq. (2). Last, the hyperprior offers a flexible z -adaptive latent prior that better models the true latent distribution than typical VAE priors. Therefore, under the formalism of Sec. 2.2 summarized in Fig. 1, the MAP- z estimate for CAEs is given by:

$$\begin{aligned} z^* &= \arg \min_z -\log p_{Y|Z}(y|z) - \log p_\theta(z) \quad (13) \\ &= \arg \min_z \|AD_\theta(z) - y\|_2^2 + \lambda \text{Rate}(z, E_{h,\phi}(z)) \end{aligned}$$

where $E_{h,\phi}(z)$ represents the output of the hyperencoder. Note that, in a proper MAP framework, both z and h should be optimized, with $-\log p_\theta(z, h) = \lambda \text{Rate}(z, h)$. As h is low-dimensional and does not significantly impact the rate, we choose the approximation $h = E_{h,\phi}(z)$. We show, in the ablation study provided in the supplementary, that this approximation does not impact the algorithm performance. It is also important to note that the MAP- z estimate in eq. (13) will not be used in practice, as we employ the variational Bayes image restoration algorithm introduced in the following section.

Another benefit of using CAE for latent optimization is the availability of trained compression models with an optimized architecture at different points of the rate-distortion trade-off, as compression is typically done at various bitrates. A small value of the parameter α , controlling that trade-off, corresponds to a low bitrate, potentially imposing a strong manifold constraint as is the case in the original latent MAP [6]. This is powerful when solving severely

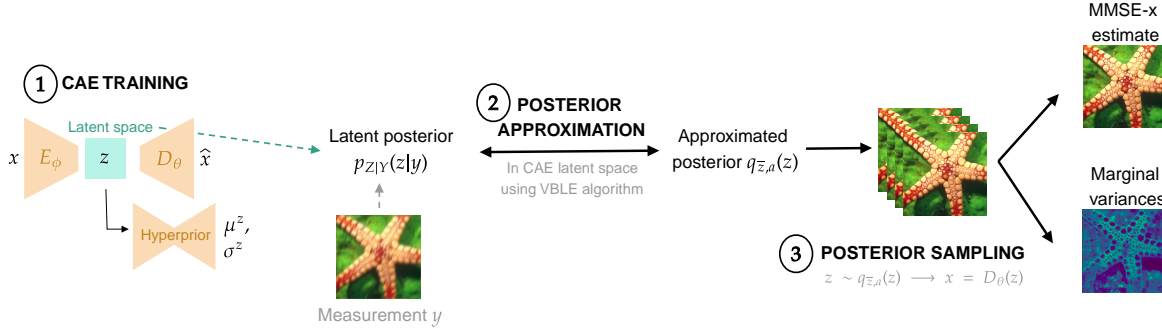


Figure 2. Overview of the image restoration process. First, a compressive autoencoder (CAE) is trained on a dataset of ideal images. Then, to restore a degraded image y , the latent posterior $p_{Z|Y}(z|y)$ is approximated using variational inference, and finally, the approximated posterior $q_{\bar{z},a}(z)$ is sampled in order to compute an MMSE estimate of the solution as well as uncertainties.

ill-posed inverse problems, but can cause significant reconstruction errors, especially if the image is slightly out-of-distribution. Therefore, for inverse problems of moderate difficulty, CAEs trained for higher bitrates should be used. Furthermore, for classical VAEs, the ELBO in (7) exhibits a similar trade-off, between the data fidelity and the KL terms. Assuming that the VAE decoder is a Gaussian with mean denoted as $D_\theta(z)$ and variance γ^2 , the trade-off is controlled by γ since the ELBO can be reformulated as follows:

$$\mathcal{L}_{\theta,\phi}(x) = \frac{1}{2\gamma^2} \|x - D_\theta(z)\|_2^2 - KL(q_\phi(z|x)||p_\theta(z)). \quad (14)$$

Training VAEs at other points in this trade-off is possible but rarely done, so that off-the-shelf VAE models with an optimized but relatively light neural structure are not available in practice, in contrast to CAEs.

3.2 Variational Bayes Latent Estimation (VBLE)

Our second contribution exploits the properties of autoencoders latent space. In the case of CAEs, recall that a uniform noise is added in the latent space during training to simulate the effect of quantization. This noise is thus related to quantization uncertainty in the image space. Exploiting this noise within the image restoration process not only has the potential to improve the optimization performance, but also enables to derive uncertainty estimates. Yet, to our knowledge, latent optimization methods do not harness this potential. Therefore, in this section, we present a stochastic version of eq. (13), termed Variational Bayes Latent Estimation (VBLE), which involves sampling steps during the gradient descent process to approximate $p_{Z|Y}(z|y)$ through variational inference. Note that VBLE can be applied with both VAEs and CAEs.

The autoencoding inference distribution takes the form of $q_\phi(z|x, h) = \prod_k \mathcal{U}(z_k; [\bar{z}_k - \frac{1}{2}, \bar{z}_k + \frac{1}{2}])$ for CAEs, and $q_\phi(z|x) = \prod_k \mathcal{N}(z_k; \bar{z}_k, \sigma_\phi(x)_k^2)$ for VAEs. As dis-

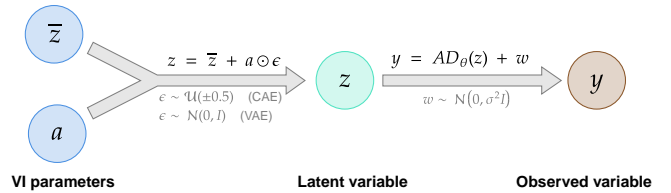


Figure 3. Variational Bayes Latent Estimation (VBLE) graph. VI stands for Variational Inference.

cussed previously, we choose to estimate only the latent variable z by setting $h \approx E_{h,\phi}(z)$, which does not lower the performance. However, note that VBLE can be easily extended to an arbitrary set of latent variables. As previously mentioned in the introduction, we consider $p_{Y|Z}(y|z) = p_{Y|X}(y|D_\theta(z))$. Bora et al. [6] method to solve inverse problems yields a MAP estimate $\arg \max_z p_{Z|Y}(z|y)$ in the latent space. Unlike this deterministic approach resulting in a point estimate, we wish to approximate $p_{Z|Y}(z|y)$ using variational inference, with an element of the parametric family:

$$E_{\bar{z},a} = \{q_{\bar{z},a}(z) | \bar{z}, a \in \mathbb{R}^{C \times M \times N}, a > 0\}$$

$$\text{where } q_{\bar{z},a}(z) = \prod_k \mathcal{U}(z_k; [\bar{z}_k - \frac{a_k}{2}, \bar{z}_k + \frac{a_k}{2}]) \quad (\text{CAE case}),$$

$$q_{\bar{z},a}(z) = \prod_k \mathcal{N}(z_k; \bar{z}_k, a_k^2) \quad (\text{VAE case}).$$

These parametric families are based on the same distribution than the inference encoder distribution $q_\phi(z|x)$, *i.e.* uniform for CAEs and Gaussian for VAEs. Their parameters are the mean latent representation \bar{z} , and an additional a parameter with the same dimensions as \bar{z} , which models the uncertainty related to each coefficient of z .

Then, as illustrated in Fig. 3, we use variational inference to estimate (\bar{z}, a) in the same way as the VAE training procedure described in section 2.1. Hence, we maximize

the ELBO:

$$\begin{aligned} \arg \max_{\bar{z}, a} \mathcal{L}_{\bar{z}, a} &= \arg \max_{\bar{z}, a} \mathbb{E}_{q_{\bar{z}, a}(z)} [\log p_{Y|Z}(y|z) \\ &\quad + \log p_{\theta}(z) - \log q_{\bar{z}, a}(z)] \end{aligned} \quad (15)$$

with $\log p_{\theta}(z)$ being the log-likelihood of the latent prior, that is in particular $\log \mathcal{N}(z; 0, I)$ for a traditional VAE, and $\log(2)$ Rate($z, E_{h, \phi}(\bar{z})$) for a CAE with a hyperprior, as introduced in eq. (13). Note that $\log q_{\bar{z}, a}(z) = -\sum_k \log a_k$ up to a constant in both Gaussian and uniform cases. We can then use the following reparameterization, for $z \sim q_{\bar{z}, a}(z)$,

$$z = \begin{cases} \bar{z} + a \odot \epsilon \text{ with } \epsilon \sim \prod_k \mathcal{U}(\epsilon_k; [-\frac{1}{2}, \frac{1}{2}]) & \text{(CAE case)} \\ \bar{z} + a \odot \epsilon \text{ with } \epsilon \sim \mathcal{N}(0, I) & \text{(VAE case)} \end{cases}$$

where \odot denotes the Hadamard, point-wise product between two tensors.

Algorithm 1 Variational Bayes Latent Estimation

Require: $\bar{z}_0 \in \mathbb{R}^{C \times M \times N}$, $a_0 \in \mathbb{R}^{C \times M \times N} = (1)_{i,j,l}$, $k = 0$, $\eta > 0$
while not *convergence* **do**
 $z \sim q_{\bar{z}_k, a_k}(z)$
 $\begin{pmatrix} \bar{z}_{k+1} \\ a_{k+1} \end{pmatrix} = \begin{pmatrix} \bar{z}_k \\ a_k \end{pmatrix} - \eta \nabla_{\bar{z}, a} [-\log p_{Y|Z}(y|z) - \log p_{\theta}(z) + \log q_{\bar{z}, a}(z)]$
 $k = k + 1$
end while
return $(\bar{z}^*, a^*) = (\bar{z}_k, a_k)$

Therefore, given the optimal parameters (\bar{z}^*, a^*) , the distribution $q_{\bar{z}^*, a^*}(z)$ is supposed to approximate the posterior $p_{Z|Y}(z|y)$. Then, two point estimates can be derived for the restored image:

$$x_{MMSE-z}^* = D_{\theta}(\bar{z}^*), \quad (16)$$

$$x_{MMSE-x}^* = \frac{1}{L} \sum_{i=1}^L D_{\theta}(z_i) \text{ with } z_i \sim q_{\bar{z}^*, a^*}(z_i). \quad (17)$$

Both MMSE-x and MMSE-z estimates are relevant and can be used in practice.

It is important to note that the optimization procedure does not increase the restoration time compared to the classical deterministic gradient descent, and sampling afterwards from the approximation of $p_{X|Y}$ is fast and straightforward, whereas MCMC techniques require a substantial number of iterations.

4 Numerical experiments

This section presents numerical experiments to evaluate VBLE using CAEs compared to state-of-the-art baselines. First, we detail the experimental setup. Then, the quality of

the image point estimates are assessed through both quantitative and qualitative evaluations. Additionally, we analyze the efficiency of the uncertainty prediction of VBLE before a concise discussion involving the experiments.

4.1 Experimental setup

Inverse problem details. All experiments in this section are performed on subsets of BSD500 [39] and FFHQ [34] test datasets, both subsets composed of 47 images of size 256×256 . VBLE and the baselines are evaluated on three inverse problems: deblurring, single image super resolution (SISR), and inpainting. For deblurring, two Gaussian kernels of standard deviation $\sigma_k \in \{1, 3\}$ are tested, as well as a motion blur kernel, for several Gaussian noise levels. We consider the noiseless case for SISR and inpainting. SISR $\times 2$ and $\times 4$ is conducted with bicubic downsampling. We employ a 50% random mask for inpainting experiments.

Metrics. For quantitative experiments, we employ the Peak Signal-to-Noise Ratio (PSNR), the Structural Similarity [53] (SSIM) and the Learned Image Patch Similarity [57] (LPIPS) metrics. The PSNR quantifies the accuracy of the restoration between the restored and ground truth images while SSIM and LPIPS are respectively classical and network based perceptual metrics between the two images.

Compressive autoencoder details. We employ pre-trained networks from the compressAI [8] library at different bitrates. We choose two models, from Minnen and al. [40], denoted as mbt, and Cheng and al.[12], denoted as cheng. mbt is a CAE with an hyperprior combining a second autoencoder with an autoregressive model, but its encoder and decoder structures remain simple CNNs. cheng retains the same structure as mbt, but with more elaborate encoders and decoders as they possess self-attention layers, yielding state-of-the-art compression results. The networks from compressAI are pretrained on natural images. We fine-tune them for about 100k iterations on BSD and FFHQ train datasets.

VBLE parameter settings. For VBLE using CAEs, the network with the most appropriate bitrate needs to be chosen for each inverse problem. For mbt and cheng, we have trained models at 7 different bitrates. The bitrate parameter α to choose, as well as the regularization parameter λ are tuned by a grid search algorithm on a defined 3 image validation set for each dataset. The other parameters are fixed, in particular, we use Adam optimizer with learning rate 0.1 during 1000 iterations for all restoration tasks. Lastly, the MMSE-x estimate is used for all comparisons as it yielded the best results.

Baselines. We compare our method with PnP methods DPIP [55] and PnP-ADMM [52], the diffusion-based method DiffPIP [58] and the MCMC approach PnP-ULA [37]. DRUNet denoiser [55] is used for both PnP approaches and PnP-ULA. We use an available version of

BSD - deblur		Gaussian $\sigma_k = 1$			Gaussian $\sigma_k = 3$			Motion		
Method		PSNR \uparrow	LPIPS \downarrow	SSIM \uparrow	PSNR \uparrow	LPIPS \downarrow	SSIM \uparrow	PSNR \uparrow	LPIPS \downarrow	SSIM \uparrow
Bayesian	VBLE (cheng)	29.77	<u>0.2002</u>	<u>0.8617</u>	<u>24.55</u>	<u>0.4030</u>	0.6346	<u>28.56</u>	<u>0.2466</u>	<u>0.8163</u>
	VBLE (mbt)	29.59	0.2006	0.8587	24.41	0.4147	0.6231	28.31	0.2488	0.8095
Punctual	PnP-ULA	27.71	0.2675	0.7809	23.75	0.4592	0.5913	27.17	0.2643	0.7402
	DPIR	<u>29.72</u>	<u>0.2127</u>	0.8623	24.41	0.4315	0.6427	28.69	0.2606	0.8285
	PnP-ADMM	28.96	0.2155	0.8456	24.24	0.4350	0.6333	28.16	0.3349	0.8045
	DiffPIR	29.26	0.1832	0.8420	24.58	0.3605	<u>0.6405</u>	28.15	0.2230	0.7955

FFHQ - deblur		Gaussian $\sigma_k = 1$			Gaussian $\sigma_k = 3$			Motion		
Method		PSNR \uparrow	LPIPS \downarrow	SSIM \uparrow	PSNR \uparrow	LPIPS \downarrow	SSIM \uparrow	PSNR \uparrow	LPIPS \downarrow	SSIM \uparrow
Bayesian	VBLE (cheng)	<u>34.34</u>	0.1440	<u>0.9186</u>	29.49	0.2755	<u>0.8183</u>	<u>32.08</u>	0.2010	<u>0.8751</u>
	VBLE (mbt)	34.21	0.1600	0.9177	28.70	0.3212	0.7686	31.97	0.2149	0.8741
Punctual	PnP-ULA	32.51	0.2014	0.8811	28.40	0.3248	0.7891	30.35	0.2367	0.7833
	DPIR	34.81	0.1244	0.9265	29.11	0.2301	0.8228	32.72	0.1518	0.8920
	PnP-ADMM	33.91	0.1463	0.9146	28.06	<u>0.2431</u>	0.8113	30.71	0.1966	0.8563
	DiffPIR	33.92	<u>0.1368</u>	0.9049	<u>29.41</u>	0.2691	0.8102	31.98	<u>0.1793</u>	0.8677

Table 1. Deblurring results on BSD and FFHQ dataset, Gaussian noise with $\sigma = 7.65/255$. Best result in bold font, second underlined.

BSD		SISR $\times 2$			SISR $\times 4$			Inpainting		
Method		PSNR \uparrow	LPIPS \downarrow	SSIM \uparrow	PSNR \uparrow	LPIPS \downarrow	SSIM \uparrow	PSNR \uparrow	LPIPS \downarrow	SSIM \uparrow
Bayesian	VBLE (cheng)	29.63	0.1847	0.8749	25.44	<u>0.3516</u>	0.6945	30.45	0.1247	0.9091
	VBLE (mbt)	<u>29.56</u>	0.1830	0.8749	25.05	0.3730	0.6802	30.80	0.1146	0.9165
Punctual	PnP-ULA	28.42	0.1659	0.8763	24.82	0.3730	0.6894	26.29	0.2497	0.8122
	DPIR	29.55	<u>0.1706</u>	0.8784	<u>25.18</u>	<u>0.3652</u>	<u>0.6937</u>	<u>31.58</u>	0.0659	<u>0.9316</u>
	PnP-ADMM	29.31	0.1907	0.8678	24.77	0.4227	<u>0.6659</u>	31.69	<u>0.0675</u>	0.9322
	DiffPIR	29.20	0.1645	0.8539	25.03	0.3164	0.6771	30.41	0.0919	0.9018

FFHQ -		SISR $\times 2$			SISR $\times 4$			Inpainting		
Method		PSNR \uparrow	LPIPS \downarrow	SSIM \uparrow	PSNR \uparrow	LPIPS \downarrow	SSIM \uparrow	PSNR \uparrow	LPIPS \downarrow	SSIM \uparrow
Bayesian	VBLE (cheng)	<u>36.32</u>	0.0995	<u>0.9516</u>	31.26	0.2048	0.8699	36.98	0.0795	0.9623
	VBLE (mbt)	35.99	0.0956	0.9514	<u>31.01</u>	0.2258	<u>0.8680</u>	37.04	0.0738	0.9643
Punctual	PnP-ULA	30.82	0.1570	0.8599	28.94	0.2495	0.8508	34.77	0.1293	0.9349
	DPIR	36.47	<u>0.0955</u>	0.9535	30.93	<u>0.1956</u>	0.8660	<u>37.65</u>	<u>0.0466</u>	<u>0.9710</u>
	PnP-ADMM	35.23	0.0920	0.9446	30.76	0.1920	0.8654	38.77	0.0394	0.9750
	DiffPIR	34.94	0.1089	0.9269	30.71	0.2042	0.8492	36.08	0.0653	0.9470

Table 2. Super resolution and inpainting results on BSD and FFHQ datasets. Best result in bold font, second underlined.

Method	DPIR	DiffPIR	PnP-ULA	VBLE (cheng)	VBLE (mbt)
Used neural network	DRUNet	Diffusion model	DRUNet	CAE	CAE
Network number of parameters	32M	93M (FFHQ) 552M (BSD)	32M	29M	14M-25M
Restoration time	3s	21s	1h23m29s	24s	11s

Table 3. Computational load for the different methods. Computation time is given for inpainting one BSD image on a Nvidia Quadro RTX 8000 GPU. For mbt number of parameters, 14M correspond to low bitrate networks, 25M to high bitrates.

DRUNet trained on BSD [55] and we train it for FFHQ dataset with standard hyperparameters. For DiffPIR, we use an available FFHQ pretrained diffusion model [13] and a pretrained model on ImageNet [20], that we finetune on BSD dataset. For PnP-ULA, 10^5 MCMC iterations are performed. Particular attention has been given to tuning hyperparameters of each method in the same way, on the same 3 image subset as VBLE. Detailed experimental settings are available on section 6.3. of the supplementary material.

4.2 Results

Tables 1 and 2 show quantitative results on several inverse problems. A distinction is made between Bayesian methods which enable posterior sampling and punctual methods which only provide a single estimate. Except PnP-ULA which remains slightly below, all methods often exhibit similar performance on the majority of inverse prob-

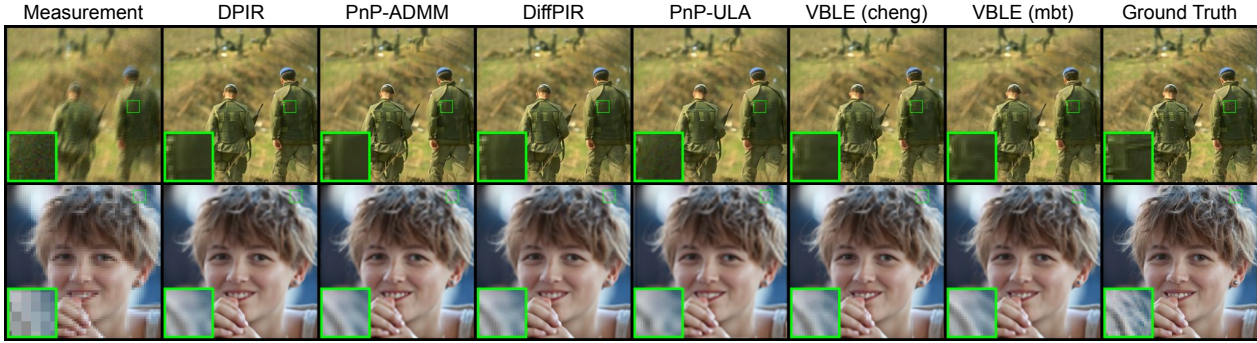


Figure 4. Qualitative results for image restoration. Top: motion deblurring ($\sigma = 7.65/255$). Bottom: SISR $\times 4$

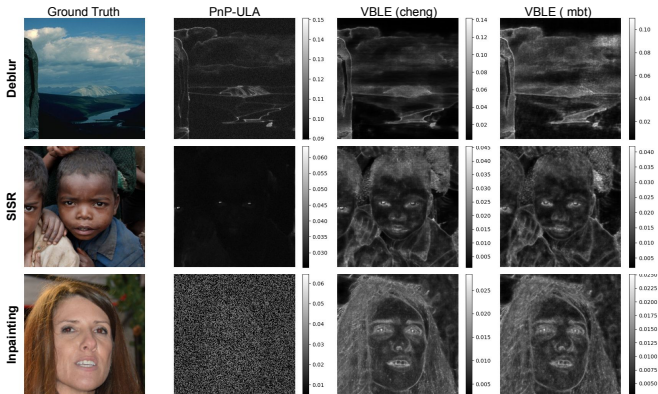


Figure 5. Marginal standard deviations, representing the uncertainty, for VBLE and PnP-ULA. 100 posterior samples are used for VBLE, PnP-ULA standard deviation are regularly updated during the iterations after a burn-in period.

lems. In particular, VBLE exhibits good performance as it reaches the first or second rank for a majority of inverse problems and metrics. VBLE often outperforms the baselines for SISR, is competitive for deblurring and seems, as DiffPIR, slightly below PnP methods for inpainting. Overall, VBLE clearly outperforms PnP-ULA, which is the only other posterior sampling method. Visual results are given on Fig. 4 and in the supplementary material. Although all methods perform relatively well, PnP methods and DiffPIR appear to flatten images and tend to hallucinate, whereas VBLE gives more textures and remains faithful, sometimes at the cost of keeping some degradation residue.

Finally, these results have to be considered within the insights of Tab. 3. In particular, the restoration process is several orders of magnitude longer for PnP-ULA than for the other methods, even though PnP-ULA computation time can sometimes be reduced by lowering the number of iterations.

4.3 Uncertainty visualization

Marginal posterior standard deviations are displayed on Fig. 5. First, VBLE yields, in average, lower standard deviations than PnP-ULA. This can partly arise from the fact that VBLE provides better point estimates. Then, for low frequency zones, VBLE seems almost certain of its prediction in contrast to PnP-ULA. Yet, inpainting predictions significantly differ between the two methods. PnP-ULA’s marginal variance seems to follow the mask for the inpainting problem. In contrast, VBLE’s uncertainties seem independent of the mask, and thus less accurate. This might be explained by the variational distribution chosen to approximate the posterior. While the a parameter is supposed to capture the uncertainty for each coefficient of z , this is done in the latent space and thus at a coarse scale. Hence, it does not account for the fine scale of the random mask.

4.4 Discussion

The key result in section 4 is thus that VBLE using CAEs reaches state-of-the-art point estimation results for image restoration, while deriving uncertainties in a fast and efficient manner. The predicted variances seem relevant for deblurring and SISR, and more generally should be appropriate for inverse problems for which the uncertainties are likely to stay regular. A careful analysis of VBLE marginal variances can be found in the supplementary material as well as a thorough ablation study.

The fact that VBLE does not tend to hallucinate combined with its posterior sampling ability is an important feature of VBLE using CAEs. Compared to alternative methods from the literature, VBLE thus seems a relevant option for real applications such as satellite image restoration, for which introducing artifacts must be avoided.

5 Conclusion

To conclude, we introduced the VBLE algorithm, which performs variational inference in the latent space of a variational (compressive) autoencoder. It allows for an efficient

approximation of the posterior distribution associated to an image restoration task. In our experiments, VBLE using compressive autoencoders achieve state-of-the-art results and provide accurate estimations of the uncertainty. The proposed approach thus bridges the performance gap between latent optimization and PnP methods for the restoration of non-structured images, with similar or lighter networks than typical Gaussian denoisers or diffusion models.

Further work will be dedicated to improve the performance of VBLE, by considering more expressive variational distribution families or by a joint estimation in the latent and image space [27, 23]. Another key perspective is to consider modulated CAEs [49] which allow to compress at multiple bit-rates, thus enabling to regularize inverse problems of various difficulties with a single neural network.

Acknowledgments

This work was partly supported by CNES under project name DEEPREG, and ANITI under grant agreement ANR-19-PI3A-0004.

References

- [1] M. Asim, M. Daniels, O. Leong, A. Ahmed, and P. Hand. Invertible generative models for inverse problems: mitigating representation error and dataset bias. In *International Conference on Machine Learning (ICML)*, pages 399–409. PMLR, 2020.
- [2] J. Ballé, V. Laparra, and E. P. Simoncelli. Density modeling of images using a generalized normalization transformation. In *International Conference on Learning Representations (ICLR)*, 2016.
- [3] J. Ballé, V. Laparra, and E. P. Simoncelli. End-to-end optimized image compression. In *International Conference of Learning Representations (ICLR)*, 2017.
- [4] J. Ballé, D. Minnen, S. Singh, S. J. Hwang, and N. Johnston. Variational image compression with a scale hyperprior. In *International Conference of Learning Representations (ICLR)*, 2018.
- [5] D. M. Blei, A. Kucukelbir, and J. D. McAuliffe. Variational inference: A review for statisticians. *Journal of the American statistical Association*, 112:859–877, 2017.
- [6] A. Bora, A. Jalal, E. Price, and A. G. Dimakis. Compressed sensing using generative models. In *International Conference on Machine Learning (ICML)*, 2017.
- [7] A. C. Bovik. *Handbook of image and video processing*. Academic press, 2010.
- [8] J. Bégin, F. Racapé, S. Feltman, and A. Pushparaja. CompressAI: a PyTorch library and evaluation platform for end-to-end compression research. *arXiv preprint arXiv:2011.03029*, 2020.
- [9] Z. Cai, J. Tang, S. Mukherjee, J. Li, C. B. Schönlieb, and X. Zhang. NF-ULA: Langevin Monte Carlo with Normalizing Flow Prior for Imaging Inverse Problems. *arXiv preprint arXiv:2304.08342*, 2023.
- [10] S. H. Chan, X. Wang, and O. A. Elgendy. Plug-and-play ADMM for image restoration: Fixed-point convergence and applications. *IEEE Transactions on Computational Imaging*, 3(1):84–98, 2016.
- [11] Z. Chen, W. Guo, Y. Feng, Y. Li, C. Zhao, Y. Ren, and L. Shao. Deep-learned regularization and proximal operator for image compressive sensing. *IEEE Transactions on Image Processing*, 30:7112–7126, 2021.
- [12] Z. Cheng, H. Sun, M. Takeuchi, and J. Katto. Learned image compression with discretized gaussian mixture likelihoods and attention modules. In *IEEE Conference on Computer Vision and Pattern Recognition (CVPR)*, 2020.
- [13] J. Choi, S. Kim, Y. Jeong, Y. Gwon, and S. Yoon. ILVR: Conditioning method for denoising diffusion probabilistic models. In *IEEE/CVF International Conference on Computer Vision (ICCV)*, pages 14347–14356, 2021.
- [14] H. Chung, J. Kim, M. T. McCann, M. L. Klasky, and J. C. Ye. Diffusion posterior sampling for general noisy inverse problems. In *International Conference on Learning Representations (ICLR)*, 2023.
- [15] F. Coeurdoux, N. Dobigeon, and P. Chainais. Plug-and-play split gibbs sampler: embedding deep generative priors in bayesian inference. *arXiv preprint arXiv:2304.11134*, 2023.
- [16] G. Daras, A. Odena, H. Zhang, and A. G. Dimakis. Your local GAN: Designing two dimensional local attention mechanisms for generative models. In *IEEE/CVF conference on computer vision and pattern recognition (CVPR)*, pages 14531–14539, 2020.
- [17] V. A. de Oliveira, M. Chabert, T. Oberlin, C. Poulliat, M. Bruno, C. Latry, M. Caravan, S. Henrot, F. Falzon, and R. Camarero. Satellite image compression and denoising with neural networks. *IEEE Geoscience and Remote Sensing Letters*, 19:1–5, 2022.
- [18] J. Dean, G. Daras, and A. Dimakis. Intermediate layer optimization for inverse problems using deep generative models. In *NeurIPS 2020 Workshop on Deep Learning and Inverse Problems*, 2020.
- [19] M. Dhar, A. Grover, and S. Ermon. Modeling sparse deviations for compressed sensing using generative models. In *International Conference on Machine Learning (ICLR)*, pages 1214–1223. PMLR, 2018.
- [20] P. Dhariwal and A. Nichol. Diffusion models beat GANs on image synthesis. *Advances in Neural Information Processing Systems (NeurIPS)*, 34:8780–8794, 2021.
- [21] L. Dinh, D. Krueger, and Y. Bengio. NICE: Non-linear independent components estimation. In *International Conference of Learning Representations (ICLR)*, 2015.
- [22] C. Dong, C. C. Loy, K. He, and X. Tang. Learning a deep convolutional network for image super-resolution. *European Conference on Computer Vision (ECCV)*, pages 184–199, 2014.

- [23] M. Duff, N. D. F. Campbell, and M. J. Ehrhardt. Regularising inverse problems with generative machine learning models. *Journal of Mathematical Imaging and Vision*, 2023.
- [24] M. A. Duff, I. J. Simpson, M. J. Ehrhardt, and N. D. Campbell. VAEs with structured image covariance applied to compressed sensing mri. *Physics in Medicine & Biology*, 68(16):165008, 2023.
- [25] A. Durmus, E. Moulines, and M. Pereyra. Efficient bayesian computation by proximal Markov chain Monte Carlo: when Langevin meets Moreau. *SIAM Journal on Imaging Sciences*, 11(1):473–506, 2018.
- [26] M. Elad. *Sparse and Redundant Representations: From Theory to Applications in Signal and Image Processing*, volume 2. Springer, 2010.
- [27] M. González, A. Almansa, and P. Tan. Solving inverse problems by joint posterior maximization with autoencoding prior. *SIAM Journal on Imaging Sciences*, 15(2):822–859, 2022.
- [28] N. Hansen. The CMA Evolution Strategy: A tutorial. *arXiv preprint arXiv:1604.00772*, 2016.
- [29] J. Ho, A. Jain, and P. Abbeel. Denoising diffusion probabilistic models. *Advances in Neural Information Processing Systems (NeurIPS)*, 2020.
- [30] M. Holden, M. Pereyra, and K. C. Zygalakis. Bayesian imaging with data-driven priors encoded by neural networks. *SIAM Journal on Imaging Sciences*, 15(2):892–924, 2022.
- [31] S. Hurault, A. Leclaire, and N. Papadakis. Gradient step denoiser for convergent plug-and-play. In *International Conference on Learning Representations (ICLR)*, 2022.
- [32] Z. Kadkhodaie and E. Simoncelli. Stochastic solutions for linear inverse problems using the prior implicit in a denoiser. *Advances in Neural Information Processing Systems*, 34:13242–13254, 2021.
- [33] U. S. Kamilov, H. Mansour, and B. Wohlberg. A plug-and-play priors approach for solving nonlinear imaging inverse problems. *IEEE Signal Processing Letters*, 24(12):1872–1876, 2017.
- [34] T. Karras, S. Laine, and T. Aila. A style-based generator architecture for generative adversarial networks. In *IEEE/CVF conference on computer vision and pattern recognition (CVPR)*, pages 4401–4410, 2019.
- [35] B. Kwar, M. Elad, S. Ermon, and J. Song. Denoising diffusion restoration models. *Advances in Neural Information Processing Systems (NeurIPS)*, 35:23593–23606, 2022.
- [36] D. P. Kingma and M. Welling. Auto-encoding variational bayes. In *International Conference on Learning Representations (ICLR)*, 2014.
- [37] R. Laumont, V. D. Bortoli, A. Almansa, J. Delon, A. Durmus, and M. Pereyra. Bayesian Imaging using plug & play priors: when Langevin meets Tweedie. *SIAM Journal on Imaging Sciences*, 15(2):701–737, 2022.
- [38] S. Mallat. Wavelet tour of signal processing: The sparse way, 2008.
- [39] D. Martin, C. Fowlkes, D. Tal, and J. Malik. A database of human segmented natural images and its application to evaluating segmentation algorithms and measuring ecological statistics. In *IEEE International Conference on Computer Vision (ICCV)*, volume 2, pages 416–423 vol.2, 2001.
- [40] D. Minnen, J. Ballé, and G. D. Toderici. Joint autoregressive and hierarchical priors for learned image compression. In *Advances in neural information processing systems (NeurIPS)*, volume 31, 2018.
- [41] A. Q. Nichol and P. Dhariwal. Improved denoising diffusion probabilistic models. In *International Conference on Machine Learning (ICML)*, pages 8162–8171. PMLR, 2021.
- [42] T. Oberlin and M. Verm. Regularization via deep generative models: an analysis point of view. In *International Conference on Image Processing (ICIP)*, pages 404–408. IEEE, 2021.
- [43] M. Pereyra, L. V. Mieleles, and K. C. Zygalakis. Accelerating Proximal Markov Chain Monte Carlo by Using an Explicit Stabilized Method. *SIAM Journal on Imaging Sciences*, 13(2):905–935, 2020.
- [44] J. Prost, A. Houdard, A. Almansa, and N. Papadakis. Inverse problem regularization with hierarchical variational autoencoders. In *IEEE International Conference on Computer Vision (ICCV)*, 2023.
- [45] L. I. Rudin, S. Osher, and E. Fatemi. Nonlinear total variation based noise removal algorithms. *Physica D: Nonlinear Phenomena*, 1992.
- [46] C. Saharia, J. Ho, W. Chan, T. Salimans, D. J. Fleet, and M. Norouzi. Image super-resolution via iterative refinement. *IEEE Transactions on Pattern Analysis and Machine Intelligence*, 45(4):4713–4726, 2022.
- [47] A. Skodras, C. Christopoulos, and T. Ebrahimi. The jpeg 2000 still image compression standard. *IEEE Signal processing magazine*, 18(5):36–58, 2001.
- [48] C. K. Sonderby, T. Raiko, L. Maaloe, S. K. Sonderby, and O. Winther. Ladder variational autoencoders. In D. Lee, M. Sugiyama, U. Luxburg, I. Guyon, and R. Garnett, editors, *Advances in Neural Information Processing Systems*, volume 29. Curran Associates, Inc., 2016.
- [49] M. Song, J. Choi, and B. Han. Variable-rate deep image compression through spatially-adaptive feature transform. In *IEEE/CVF International Conference on Computer Vision (ICCV)*, pages 2380–2389, 2021.
- [50] R. Tibshirani. Regression shrinkage and selection via the lasso. *Journal of the Royal Statistical Society: Series B (Methodological)*, 1996.
- [51] A. Tikhonov. Solution of incorrectly formulated problems and the regularization method. *Soviet Math.*, 1963.
- [52] S. V. Venkatakrisnan, C. A. Bouman, and B. Wohlberg. Plug-and-play priors for model based reconstruction. *IEEE Global Conference on Signal and Information Processing (GlobalSIP)*, 2013.

- [53] Z. Wang, A. C. Bovik, H. R. Sheikh, and E. P. Simoncelli. Image quality assessment: from error visibility to structural similarity. *IEEE transactions on image processing*, 13(4):600–612, 2004.
- [54] P. A. Wintz. Transform picture coding. *Proceedings of the IEEE*, 60(7):809–820, 1972.
- [55] K. Zhang, Y. Li, W. Zuo, L. Zhang, L. Van Gool, and R. Timofte. Plug-and-play image restoration with deep denoiser prior. *IEEE Transactions on Pattern Analysis and Machine Intelligence*, 44(10):6360–6376, 2021.
- [56] K. Zhang, W. Zuo, S. Gu, and L. Zhang. Learning deep CNN denoiser prior for image restoration. In *IEEE conference on computer vision and pattern recognition (CVPR)*, pages 3929–3938, 2017.
- [57] R. Zhang, P. Isola, A. A. Efros, E. Shechtman, and O. Wang. The unreasonable effectiveness of deep features as a perceptual metric. In *IEEE/CVF Conference on Computer Vision and Pattern Recognition (CVPR)*, pages 586–595, 2018.
- [58] Y. Zhu, K. Zhang, J. Liang, J. Cao, B. Wen, R. Timofte, and L. Van Gool. Denoising diffusion models for plug-and-play image restoration. In *IEEE/CVF Conference on Computer Vision and Pattern Recognition (CVPR)*, pages 1219–1229, 2023.

Supplementary Material

A Ablation Study

For the main experiments, several choices are made. In particular, the MMSE-x estimate is preferred to the MMSE-z estimate (see Sec. 3.2), while only z is optimized as we approximate the second latent variable $h = E_{h,\phi}(\bar{z})$ (see Sec. 3.1). In this section, quantitative and qualitative results with the MMSE-z estimate and with an optimization on (z, h) are given in Tab. 4 and in Fig. 6. These experiments also include results for the deterministic counterpart MAP-z of VBLE described in eq. (13).

Method	FFHQ - SISR $\times 4$			BSD - Gaussian deblur		
	PSNR \uparrow	LPIPS \downarrow	SSIM \uparrow	PSNR \uparrow	LPIPS \downarrow	SSIM \uparrow
VBLE MMSE-x	31.44	0.2032	0.8732	24.55	0.4030	0.6346
VBLE MMSE-z	31.39	0.2296	0.8714	24.60	0.4446	0.6409
VBLE _{z,h} MMSE-x	31.44	0.2021	0.8732	24.55	0.4062	0.6346
MAP-z	31.29	0.2245	0.8719	24.42	0.4247	0.6323

Table 4. Quantitative results for different variants of our method. MMSE-x and MMSE-z denote the two possible estimators defined in Sec. 3.2. VBLE _{z,h} means that z and h have been optimized, in contrast to VBLE, where only z is optimized and $h = E_{h,\phi}(\bar{z})$ (see Sec. 3.2 for the definition). MAP-z corresponds to the deterministic counterpart defined in eq. (13). All variants have the same restoration parameters (*i.e.* same λ and α). For the Gaussian deblur experiment, $\sigma = 7.65/255$ and $\sigma_k = 3$.



Figure 6. Visual results for different variants of our method. The first row corresponds to a SISR $\times 4$ experiment on FFHQ, while the second row is Gaussian deblurring ($\sigma_k = 3$, $\sigma = 7.65/255$) on BSD. MMSE-x and MMSE-z denote the two possible estimators, as defined in Sec. 3.2. VBLE _{z,h} means that z and h have been optimized, in contrast to VBLE, where only z is optimized and $h = E_{h,\phi}(\bar{z})$ (see Sec. 3.2). MAP-z corresponds to the deterministic counterpart defined in eq. (13).

First, MAP-z does not perform as good as VBLE, which shows one interest of trying to estimate the full posterior distribution with variational inference. The optimization on (z, h) does not perform better than the optimization on z only. For that reason, we choose to optimize only on z for the main experiments, as the formulation is much simpler. At last, the MMSE-z estimate yields similar PSNR and SSIM results as the MMSE-x estimate, but exhibits always a poorer LPIPS.

Additionally, a study on VBLE hyperparameters α and λ is provided in Fig. 7.



Figure 7. Influence of hyperparameters λ (regularization parameter) and α (bitrate parameter) on VBLE algorithm. To the left, on a deblurring problem on a BSD image, to the right, on a SISR problem on a FFHQ image. λ seems a more sensitive parameter than α , hence a CAE with a single bitrate could solve a wide range of inverse problem. Furthermore, the prior on FFHQ seems to be more informative compared to BSD, which makes sense as BSD dataset structure is much harder to learn.

B Additional experimental results

B.1 Uncertainties and posterior sampling evaluation

Sec. 4.3 consists in a visual evaluation of the marginal variances for VBLE compared to PnP-ULA, but their quality are not assessed quantitatively. Such quantitative analyses are not done in practice in MCMC image restoration papers [37, 30, 15], as a rigorous approach would consist in conceiving a metric to evaluate the quantity of information contained in the posterior as a whole. This appears to be complex and such metrics have, to our knowledge, not been developed for imaging problems.

Nevertheless, for VBLE, it seems of particular importance to assess the relevance of the produced uncertainties, as the obtained posterior, in contrast to MCMC, is an approximation of the true posterior. Therefore, we choose to use an empirical way to evaluate marginal variances.

The evaluation method consists in ensuring the consistency of the predicted marginal variances, for the given approximated posterior mean. Specifically, after applying the VBLE algorithm, $q_{\bar{z}^*, a^*}(z)$ approximates $p_{Z|Y}(z|y)$. Then, we choose to model $p_{X|Y}(x|y)$ by a Gaussian distribution $p^*(x|y)$ whose parameters are estimated by posterior sampling, assuming the independence of each pixel. Hence,

$$p^*(x|y) = \mathcal{N}(x; x_{MMSE-x}^*, \Sigma^{img}) \quad (18)$$

where Σ^{img} is a diagonal matrix containing the marginal variances of each pixel of the image. Hence, if $p^*(x|y)$ is a good approximation of $p_{X|Y}(x|y)$, the ideal image x should follow $p^*(x|y)$. A classical metrics to evaluate that is the negative log-likelihood defined by

$$NLL = -\log \mathcal{N}(x; x_{MMSE-x}^*, \Sigma^{img}). \quad (19)$$

The NLL will thus increase if $p^*(x|y)$ does not correctly model the image x . It is worth noting that a posterior distribution yielding a poor MMSE estimate but adapted marginal variances get a decent NLL. Hence, this metrics mainly evaluates the calibration of the marginal variances given the MMSE estimation, thus being complementary to a point quality metrics such as PSNR or LPIPS.

Dataset	Method	Deblur $\sigma = 2.55$			Deblur $\sigma = 7.65$			SISR		Inpainting
		Gaussian $\sigma_k = 1$	Gaussian $\sigma_k = 3$	Motion	Gaussian $\sigma_k = 1$	Gaussian $\sigma_k = 3$	Motion	$\times 2$	$\times 4$	50 %
BSD	VBLE (cheng)	3.86	4.40	3.85	3.59	4.07	3.84	5.61	4.27	5.44
	VBLE (mbt)	3.03	4.89	3.35	3.39	4.01	3.60	4.89	4.88	5.84
	PnP-ULA	3.74	4.29	3.29	3.88	4.37	4.03	4.79	8.84	3.33
FFHQ	VBLE (cheng)	2.62	3.30	2.85	2.79	3.35	3.04	4.27	3.43	3.28
	VBLE (mbt)	2.46	3.95	2.77	2.84	3.63	3.21	3.64	4.81	3.35
	PnP-ULA	3.03	3.72	3.65	3.49	3.99	3.75	3.16	5.19	2.00

Table 5. Negative Log-likelihood (NLL \downarrow) scores for VBLE and PnP-ULA on various inverse problems.

Tab. 5 shows the NLL of VBLE and PnP-ULA posterior distribution for several inverse problems. VBLE yields better NLL than PnP-ULA in deblurring, while the two methods are similar in SISR and PnP-ULA has better NLL scores in inpainting. These results confirm the observations of Sec. 4.3 and show the relevance of VBLE uncertainties at least for deblurring and SISR.

Additional visual results assessing the quality of VBLE posterior sampling are shown in Fig. 8. Posterior sampled estimates offer interesting sharp details but exhibit artefacts for highly underdetermined inverse problems.

B.2 Point estimation experiments

In this section, additional deblurring results are given for the noise level $\sigma = 2.55/255$ in Tab. 6 for VBLE and all the baselines. Furthermore, extensive visual results are given in Figures 9 and 10 for BSD and FFHQ datasets.

BSD - deblur		Gaussian $\sigma_k = 1$			Gaussian $\sigma_k = 3$			Motion		
Method		PSNR \uparrow	LPIPS \downarrow	SSIM \uparrow	PSNR \uparrow	LPIPS \downarrow	SSIM \uparrow	PSNR \uparrow	LPIPS \downarrow	SSIM \uparrow
Punctual / Bayesian	VBLE (cheng)	32.05	0.1234	0.9152	<u>25.21</u>	<u>0.3676</u>	0.6738	32.37	0.1392	0.9112
	VBLE (mbt)	<u>32.08</u>	<u>0.1181</u>	<u>0.9169</u>	25.06	0.3821	0.6709	32.57	0.1394	0.9143
	PnP-ULA	30.03	0.1751	0.8707	24.60	0.4027	0.6430	31.64	0.1304	0.8941
	DPIR	32.25	0.1307	0.9187	25.12	0.3809	0.6838	33.07	<u>0.1305</u>	0.9237
	PnP-ADMM	31.21	0.1381	0.9049	24.12	0.3991	0.6667	<u>32.92</u>	0.1483	<u>0.9192</u>
	DiffPIR	31.78	0.1131	0.9045	25.30	0.3172	<u>0.6783</u>	31.80	0.1242	0.8936
FFHQ - deblur		Gaussian $\sigma_k = 1$			Gaussian $\sigma_k = 3$			Motion		
Method		PSNR \uparrow	LPIPS \downarrow	SSIM \uparrow	PSNR \uparrow	LPIPS \downarrow	SSIM \uparrow	PSNR \uparrow	LPIPS \downarrow	SSIM \uparrow
Punctual / Bayesian	VBLE (cheng)	<u>36.92</u>	0.0834	0.9518	30.29	0.2443	0.8429	35.86	0.1118	0.9371
	VBLE (mbt)	36.73	<u>0.0864</u>	0.9503	29.70	0.2807	0.8262	35.76	0.1169	0.9358
	PnP-ULA	35.33	0.1229	0.9283	29.73	0.2745	0.8248	28.95	0.1813	0.8462
	DPIR	37.33	<u>0.0864</u>	0.9553	30.00	0.2060	0.8502	36.40	0.1019	0.9433
	PnP-ADMM	33.35	0.1103	0.9363	27.43	0.2280	0.8289	<u>36.30</u>	<u>0.1032</u>	<u>0.9422</u>
	DiffPIR	36.08	0.0900	0.9356	30.75	<u>0.2149</u>	<u>0.8437</u>	34.88	0.1135	0.9155

Table 6. Deblurring results on BSD and FFHQ dataset for $\sigma = 2.55/255$. Best result in bold font, second underlined.

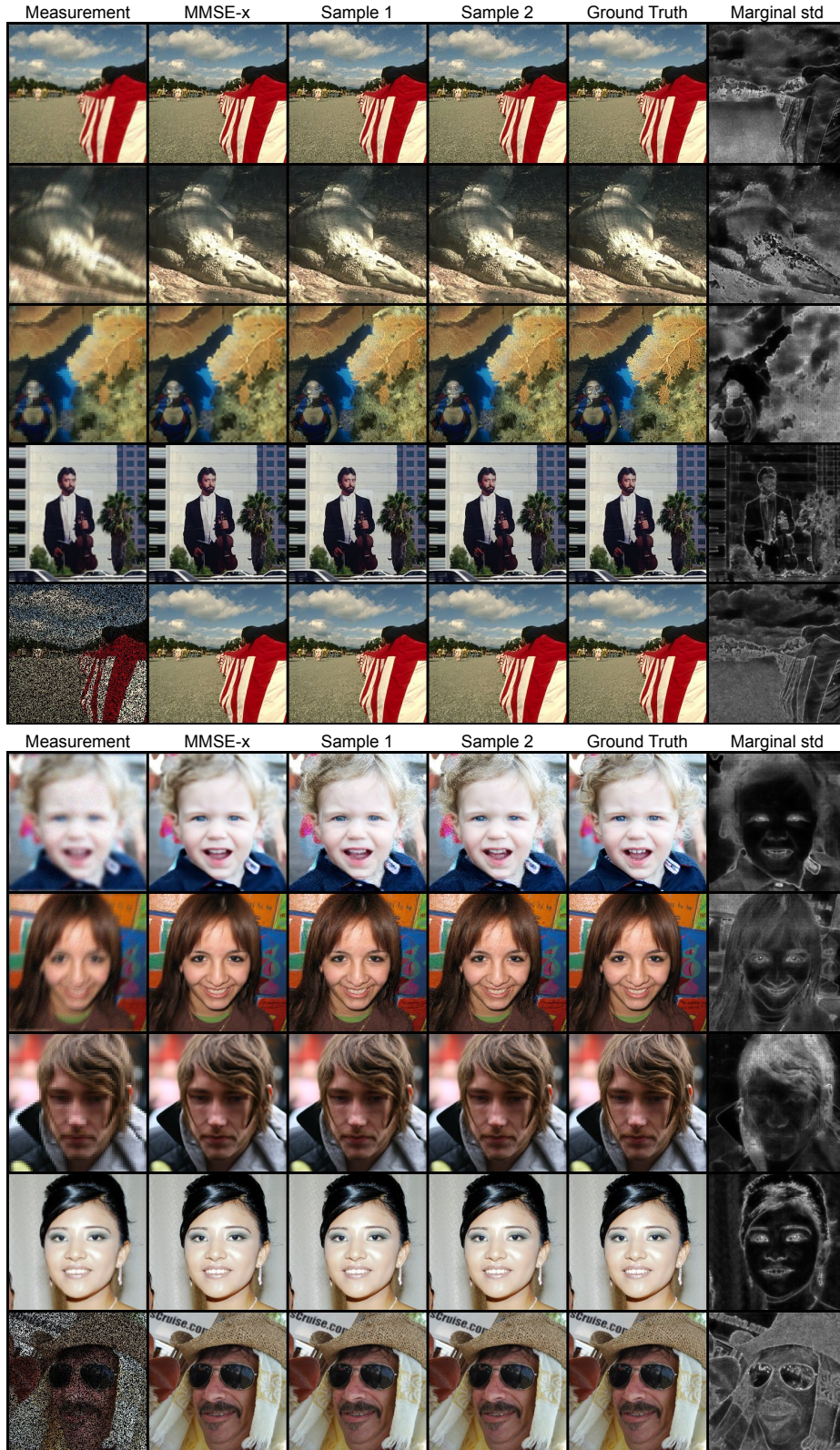


Figure 8. Posterior sampling visualisation for VBLE (cheng) for several inverse problems on BSD and FFHQ datasets. MMSE-x is the MMSE-x estimate, while sample 1 and sample 2 are sampled from the approximated posterior. Marginal std corresponds to the marginal standard deviations which have been normalized to $[0, 1]$.

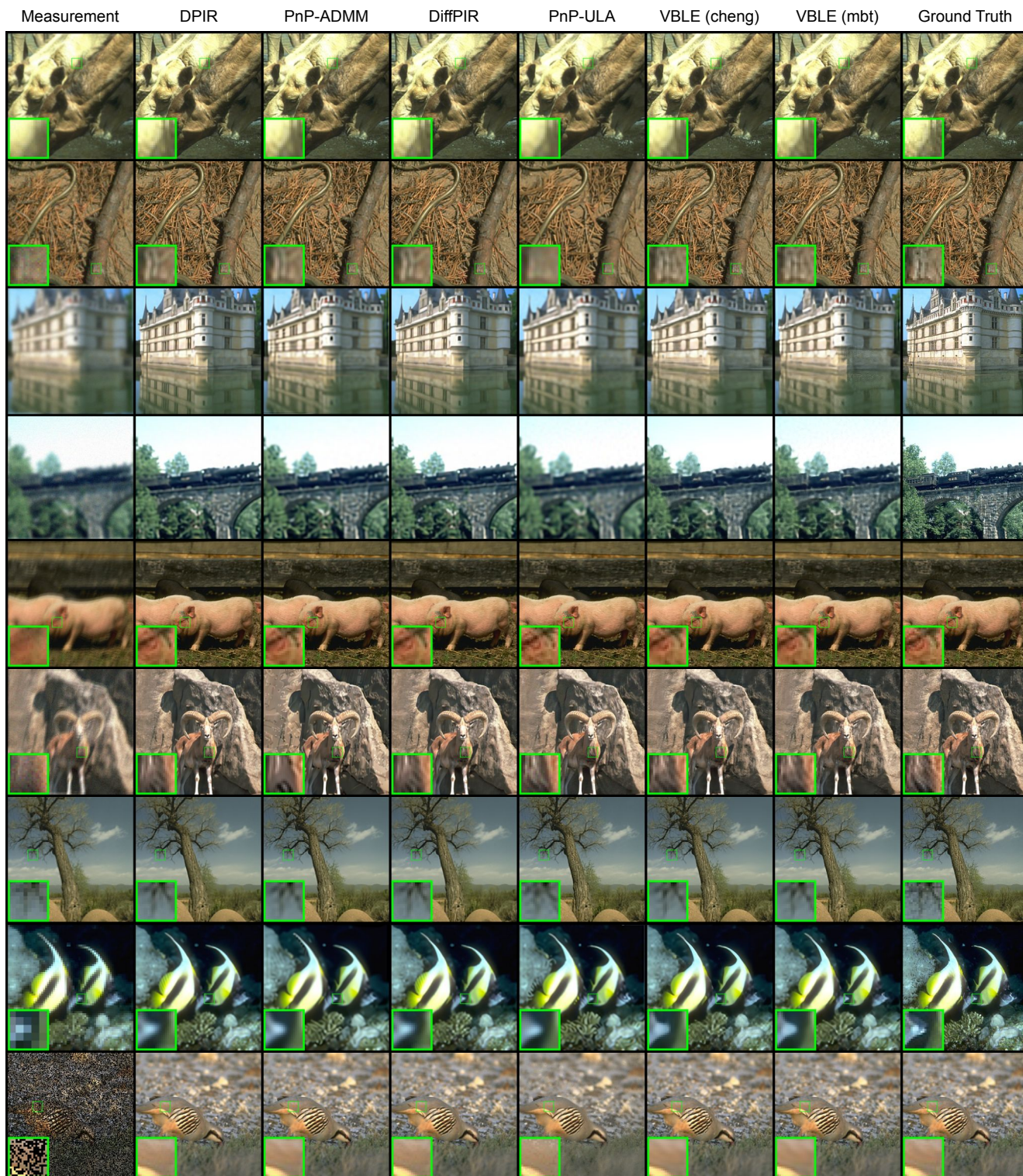
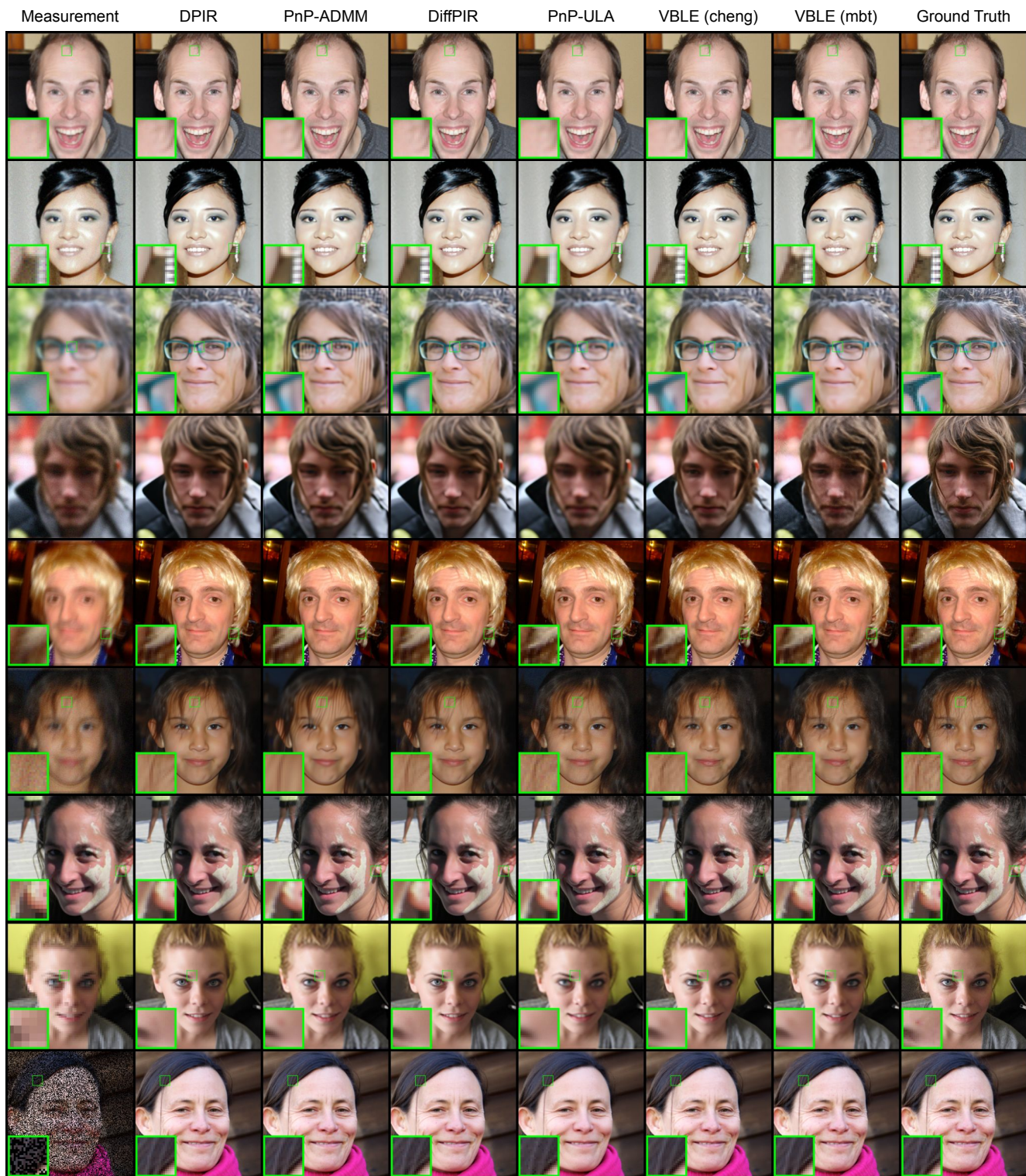


Figure 9. BSD additional visual results



C Detailed experimental setup

To tune image restoration hyperparameters of VBLE and the baselines, the same improved grid search algorithm using evolution strategies [28] has been used, except for PnP-ULA, where a classical grid search algorithm has been preferred, as the computation time was prohibitive for the other approach. In Tab. 7, the parameters which have been tuned or fixed for VBLE and each baselines are provided.

Furthermore, precise parameter settings for VBLE are available in Tab. 8.

	DPIR	PnP-ADMM	DiffPIR	PnP-ULA	VBLE
Restoration parameters details	Optimized parameters: - Regularization parameter λ - Number of iterations	Optimized parameters: - Regularization parameter λ - Number of iterations - Denoiser noise σ_D	Optimized parameters: - Regularization parameter λ - Parameter ζ Fixed parameters: - 100 denoising iterations	Optimized parameters: - Regularization parameter λ - Step size of the Markov chain - Denoiser noise σ_D Fixed parameters: - 10^5 iterations - Thinning 5 - Burn-in ratio 0.8	Optimized parameters: - Rate distortion trade-off α - Regularization parameter λ Fixed parameters: - Optimizer Adam - Learning rate $lr = 0.1$ - 1000 iterations - 100 samples for MMSE-x estimate

Table 7. Detailed experimental settings for VBLE and the baselines.

		Deblur $\sigma = 2.55/255$			Deblur $\sigma = 7.65/255$			SISR		Inpainting
		Gaussian $\sigma_k = 1$	Gaussian $\sigma_k = 3$	Motion	Gaussian $\sigma_k = 1$	Gaussian $\sigma_k = 3$	Motion	$\times 2$	$\times 4$	50%
BSD	α	0.0932	0.0067	0.0483	0.0067	0.0035	0.0067	0.025	0.0035	0.1800
	λ	8.7	19.2	9.1	82.0	81.4	75.4	5.8	8.5	20.4
cheng	α	0.0483	0.0067	0.025	0.0067	0.0035	0.0067	0.025	0.0067	0.0932
	λ	9.5	10.7	8.2	76.2	66.5	71.2	4.7	6.9	9.2
mbt	α	0.0932	0.0067	0.0483	0.013	0.0035	0.0067	0.0483	0.013	0.0932
	λ	8.9	7.8	8.1	82.9	73.6	64.8	1.1	0.62	6.2

Table 8. Detailed parameter setting for VBLE using cheng and mbt compressive networks, for all experiments in the paper. λ is the regularization parameter and α the bitrate parameter. Specifically, each CAE is trained with the loss $\mathcal{L} = 255^2 \alpha \text{Distortion} + \text{Rate}$. For mbt and cheng models, two structures, a light and a bigger one, exist [8], which are used respectively for low and high bitrates. For cheng, we have chosen the high bitrate structure for all training (even on low bitrates). For mbt, high bitrate structure has been used for high bitrate networks, and low bitrate structure for low bitrate networks.

D Similarities and differences between variational compressive autoencoders and hierarchical VAEs

In this section, CAE and traditional VAE structures are compared in order to evaluate their impact on image restoration tasks. A compressive autoencoder (CAE) with hyperprior can be expressed as a hierarchical VAE with two latent variables (z, h) . However, the inference model of CAEs with hyperprior significantly differs from usual hierarchical VAEs. A thorough visualisation of the differences between VAEs and CAEs is given in Fig. 11. First, with the formalism of Fig. 11, the posterior approximation of CAEs $q_\phi(z|x, h) = \prod_k \mathcal{U}([\bar{z}_k - \frac{1}{2}, \bar{z}_k + \frac{1}{2}]) = q_\phi(z|x)$ does not depend on h , in contrast to VAEs. Although $q_\phi(z|x)$ does not benefit from the semantic information of h in this scenario, the hyperprior operates as a self-contained entity, serving as a z -adaptive prior. Hence, the optimization on z instead of (z, h) during the image restoration process described in eq. (13) is both relevant and effective.

Then, another notable distinction is that the approximated posterior distributions of CAEs $q_\phi(z|x)$ and $q_\phi(h|x)$ are uniform with fixed variance, in contrast to Gaussian distributions with varying variance for classical VAEs. Two differences matter here: the shape of the distribution (uniform or Gaussian), and the fact that the approximated posterior has a fixed variance. In order to evaluate the impact of these differences, several VAE variants have been trained, whose validation losses are reported on Fig. 12. The idea is that neural networks with the lowest loss will yield better results in image restoration. Regarding this figure, two conclusions can be drawn:

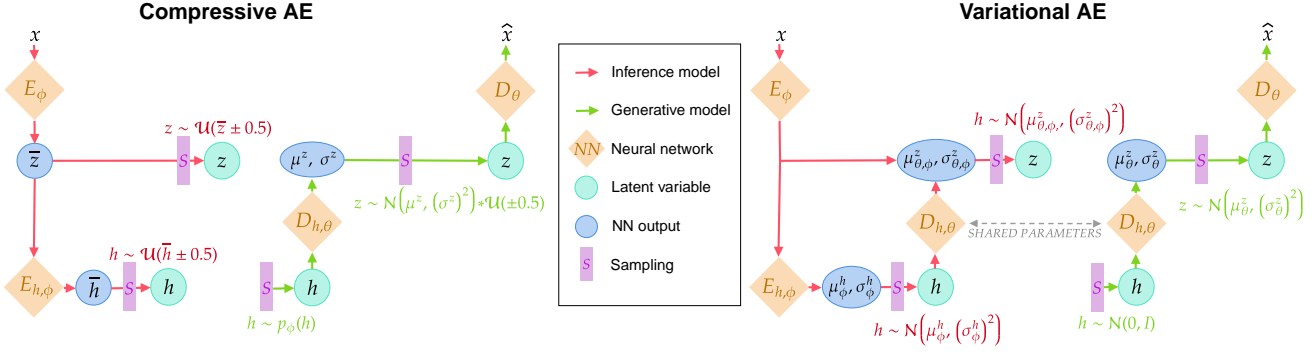


Figure 11. Comparison between compressive autoencoders and 2-latent variable VAEs. Red networks denote the inference models, green networks the generative models. The generative models are nearly the same, but significant differences lie within the inference models of VAEs and CAEs.

- as long as the variances of the prior $p_\theta(z)$ are learned as neural network parameters (learned prior (lp) versions in Fig. 12) rather than fixed, the fact that the approximated posterior has a fixed variance does not significantly impact the ELBO.
- the uniform posterior shape seems a bit less effective than the Gaussian shape, however their ELBO stay close.

Therefore, as the CAE (that is the VAE having a uniform variational distribution with a fixed variance) yields a similar ELBO as the classical VAE, we expect both architectures, CAEs and VAEs, to perform similarly for image restoration.

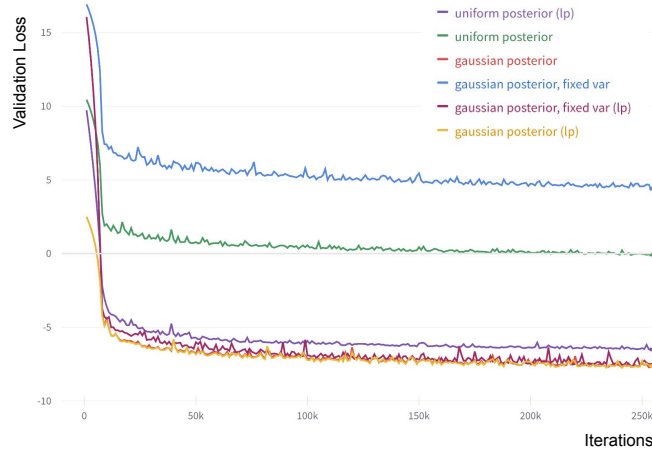


Figure 12. VAE loss $\mathcal{L} = -ELBO$ during training iterations for different VAE variants on a validation of CelebA dataset. All the models have a same simple structure with one latent variable z and have been trained with the same hyperparameters. Uniform posterior denotes a VAE with the approximated posterior $q_\phi(z|x) = \prod_k \mathcal{U}([\bar{z}_k - \frac{1}{2}, \bar{z}_k + \frac{1}{2}])$, Gaussian posterior a VAE with $q_\phi(z|x) = \prod_k \mathcal{N}((\mu_\phi^z)_k, (\sigma_\phi^z)_k^2)$, Gaussian posterior fixed var a VAE with $q_\phi(z|x) = \mathcal{N}(\mu_\phi^z, \sigma_0^2 I)$. (lp) denotes a VAE version where the prior is $p_\theta(z) = \mathcal{N}(0, \sigma_\theta^2 I)$, that is a prior whose variances are learned during the training process rather than fixed.